RSC Advances

ROYAL SOCIETY OF CHEMISTRY

PAPER

View Article Online
View Journal | View Issue

Check for updates

Cite this: *RSC Adv.*, 2023, **13**, 10068

High-performance asymmetric supercapacitor based on a $CdCO_3/CdO/Co_3O_4$ composite supported on Ni foam – part II: a three-electrode electrochemical study†

Rodrigo Henríquez, *[a] Alifhers S. Mestra-Acosta,[a] Paula Grez,[a] Eduardo Muñoz,[a] Gustavo Sessarego,[a] Elena Navarrete-Astorga [b] and Enrique A. Dalchiele[c]

Received 23rd January 2023
Accepted 17th March 2023

DOI: 10.1039/d3ra00499f

rsc.li/rsc-advances

A binder-free $CdCO_3/CdO/Co_3O_4$ compound with a micro-cube-like morphology on a nickel foam (NF) made *via* a facile two-step hydrothermal + annealing procedure has been developed. The morphological, structural and electrochemical behavior of both the single compounds constituting this final product and the final product itself has been studied. The synergistic contribution effect of the single compounds in the final compounded resulting specific capacitance values are presented and discussed. The $CdCO_3/CdO/Co_3O_4$@NF electrode exhibits excellent supercapacitive performance with a high specific capacitance (C_S) of 1.759×10^3 F g^{-1} at a current density of 1 mA cm^{-2} and a C_S value of 792.3 F g^{-1} at a current density of 50 mA cm^{-2} with a very good rate capability. The $CdCO_3/CdO/Co_3O_4$@NF electrode also demonstrates a high coulombic efficiency of 96% at a current density as high as 50 mA cm^{-2} and also exhibits a good cycle stability with capacitance retention of *ca.* 100% after 1000 cycles at a current density of 10 mA cm^{-2} along with a potential window of 0.4 V. The obtained results suggest that the facilely synthesized $CdCO_3/CdO/Co_3O_4$ compound has great potential in high-performance electrochemical supercapacitor devices.

1 Introduction

Due to both the growing request to obtain sustainable and renewable energy and intermittent energy sources such as solar and wind power, a technology that can store sustainable energy to ensure efficient, continuous, reliable and affordable energy supplies is required.[1–3] Furthermore, development of lightweight portable devices and consumer electronics has increased demand for faster sustainable energy storage systems.[1,2] Then, the main challenge is to attain an efficient and reliable electrical energy storage system, with electrochemical energy storage technologies serving as the key components.[1–3] In this way, supercapacitors (SCs) are one of the devices belonging to these electrochemical energy storage technologies, which also include batteries, conventional capacitors and fuel cells.[2] Supercapacitors are electric energy storage devices that can fill the energy/power gap between fuel cells/batteries (which have high energy storage) and conventional capacitors (which have high power output).[1,3–6] In comparison with conventional capacitors, SCs exhibit specific capacitance values from 6 to 9 orders of magnitude larger and SCs can store ten to a hundred times more energy.[7,8] In opposition to batteries, SCs can be effectively operated as advanced energy storing innovations.[7] Supercapacitors exhibit numerous appealing electrochemical merits such as: exceptional long cycle life, symmetrical (high reversibility) and sloping charge–discharge profiles, very short charge–discharge time (a few seconds), high power density and continuous variation of free energy with the conversion degree.[1,2,4,5,7,9–11] Supercapacitors are widely used in hybrid electric vehicles, portable electronic devices, medical and telecommunication devices.[8,12–14] On the basis of charge storage mechanism, SCs can be categorized into two groups: electric double layer capacitors, which use electrostatic accumulation of electrolyte ion to store energy and pseudocapacitors, which store energy by faradaic reactions.[2,11,13]

The supercapacitor (SC) electrode material (electroactive material), is the keystone component that determines the supercapacitor performance.[15–18] In fact, the performance of a SC is dependent on the intrinsic properties of the active material, *i.e.*: electronic conductivity, specific surface area, capacitance and chemical and thermal stability, and for a high-performance supercapacitor electrode material high values of

---

[a] *Instituto de Química, Facultad de Ciencias, Pontificia Universidad Católica de Valparaíso, Casilla 4059, Valparaíso, Chile. E-mail: rodrigo.henriquez@pucv.cl; Tel: +56 32 2274921*

[b] *Universidad de Málaga, Departamento de Física Aplicada I, Laboratorio de Materiales y Superficies (Unidad asociada al CSIC), E29071 Málaga, Spain*

[c] *Instituto de Física, Facultad de Ingeniería, Herrera y Reissig 565, C. C. 30, 11000 Montevideo, Uruguay*

† Electronic supplementary information (ESI) available. See DOI: https://doi.org/10.1039/d3ra00499f

these variables are desirable.[4,7] The criteria for designing a high-performance SC electrode include high specific capacitance, large rate capability and high cyclic stability, and then in its design the appropriate selection of this electrode active material is crucial.[1,4,7,10,19]

In recent years, transition metal carbonates (TMC) have been extensively investigated as a novel kind of high capacity anode material for advanced lithium-ion batteries due to their high capacities, high density, low-cost and facile operation.[20–25] For example, $CoCO_3$ could deliver an initial charge capacity as high as 1073.0 mA h g^{-1} in the voltage range 0–3.0 V,[21] and $CdCO_3$ exhibited a high initial capacity of 1251.1 mA h g^{-1}.[22] Then, TMC are considered as battery-type electrode materials.[12,26] The battery-type electrode material is considered as the key component in achieving high-performance hybrid SCs with the advantages of both: (i) supercapacitors (high power density) and (ii) advanced batteries (high energy density).[12,26] However, TMC materials exhibit the disadvantage of a poor electrical conductivity and large volume change, which lead to the loss of capacity and then limiting their practical applications.[20] Moreover, transition metal oxides (TMO) with battery behavior are considered as promising electrode materials because their theoretical capacities arising from faradaic redox reactions.[9,12,27] Among them, Co_3O_4 is seen as promising candidate owing to its: low-cost, easy synthesis, environmental friendly nature, excellent pseudo-capacitive properties (exhibiting large number of faradaic reactions among Co^{2+}/Co^{3+} and Co^{3+}/Co^{4+},[12] high specific capacitance (theoretical capacitance of $\sim$3562 F g^{-1}), structure, morphology, large surface area and electrochemical applications.[13,27–33] However, its low electrical conductivity, low electrochemical reversibility and low cycle life largely decrease its practical capacity and rate performance, and then power and energy densities are far from commercial requirements.[12,24,28] Reported values of observed specific capacitances for various Co_3O_4 SC electrode materials are well and exhaustively reviewed by Lee *et al.*,[2] with ultrahigh specific capacitance values up to 2735 F g^{-1} for mesoporous Co_3O_4 nanosheet arrays on Ni foam electrochemical supercapacitor.[34]

However, the challenge in using the above mentioned TMC and TMO compounds as SC active materials is their poor electronic conductivity. Moreover, being the electronic conductivity of the supercapacitor active material a crucial issue; in fact, a high electronic conductivity will help to maintain the rectangular nature of cyclic voltammetry curve and symmetricity of galvanostatic charging–discharging curves.[10,24,28] Furthermore, it also reduces the specific capacitance losses as potential scan rate/current densities are increased.[10,24,28] Therefore, in order to address this problem, several approaches have been reported to enhance the electronic conductivity of the SC electrode material, *i.e.*: binder-free electrode design and nanostructured current collector design to provide efficient electron pathways for charge transport,[10] synergistic effects of multiple-phase metal oxides leading to a higher electronic conductivity than those of monometallic oxides[13,27,28] and combining the active material with carbonaceous materials (or other conductive material), to enhance the electronic conductivity.[30,31,35]

An important reported optoelectronic material is constituted by cadmium oxide (CdO).[36–39] It is a post-transition metal oxide (PTMO) that crystallizes in the rock salt structure (fcc), and is characterized to exhibit a high electrical conductivity (*ca.* 5 × 10^3 S cm^{-1}) and optical transmittance in the visible region of the solar spectrum.[39–46] In this work, CdO will be employed as the electronic conductive phase that will be formed *in situ* at the expense of the previously formed $CdCO_3$.

In our research, the reasonable design of the multiphase compound integrates the battery and pseudo-capacitance character of $CdCO_3$ and Co_3O_4, respectively, and the high conductivity of CdO, leading to a $CdCO_3$/CdO/Co_3O_4 composite high-performance supercapacitor active material. Then, an enhancement of the SC electrochemical performance can be achieved because the unique properties of individual materials can be combined through a synergistic effect, *i.e.*: the composite electrodes have better electrochemical performance than either one of them individually could have. A 3D micrometer-sized networked mesoporous $CdCO_3$/CdO/Co_3O_4 composite grown directly onto nickel foam (NF) has been designed and prepared through a facile two-steps hydrothermal + annealing strategy. 3D porous architectures, because of the porosity between nanoparticles, are also crucial to enhance the surface area active materials and electrolyte transport/ion diffusion.[6,27,47–49] Furthermore, allowing the interaction with atoms, ions, and molecules not just at their surfaces, but also throughout the bulk of the materials, potentially increasing surface and interface reactions.[6,27,47,49,50] On the other hand, the active materials directly grown onto a conductive substrate is more beneficial to improve SC performance.[6,27,47,49] In fact, due to the design of the active materials direct grown on three-dimensional current collector could efficiently facilitate the transport of electrons and ions, improving the utilization of active materials, substantially increasing the power density and energy density.[6,27,47,49] For instance, NF serves both as the backbone and electron "expressway" for charge storage and delivery, overcoming the limited electrical conductivity of $CdCO_3$ and Co_3O_4 themselves.

The good performance of this multiphase $CdCO_3$/CdO/Co_3O_4 compound as an efficient active electrode material (tested in a two-electrode supercapacitor device), has been reported in our previously published paper.[51] Two-electrode test and packaged cells differ from three-electrode cells in several important aspects. The two-electrode setup is appropriate for fully assembled cells and it will more closely represent the performance of the final design.[15,17,52–56] A three-electrode setup is able to describe the electrochemical behavior of a tested material more properly than a two-electrode cell can, as is useful for a careful examination of the electrochemical properties (*i.e.*: window of voltage stability or potential-specific redox reactions), of the electrode material.[15,17,52–56]

In this work, an exhaustive three-electrode electrochemical study of this multiphase $CdCO_3$/CdO/Co_3O_4 compound has been carried out.

2 Experimental methods

2.1 Materials

Commercial nickel foam (thickness: 1.1 mm, volume density: 0.45 g cm^{-3}, average pore diameter: 13.1 mm, PPI: 95–110, porosity: 95%, specific surface areal density: 330 ± 10 g m^{-2}) was supplied by Career Henan Chemical Co., Ltd (China). Cobalt nitrate hexahydrate ($Co(NO_3)_2 \cdot 6H_2O$, ≥98.8%), cadmium nitrate hexahydrate ($Cd(NO_3)_2 \cdot 6H_2O$, ≥ 99%), urea (≥99.5%) and sodium hydroxide (KOH, ≥90%) have been purchased from Sigma-Aldrich (USA). All chemicals were used as received without further purification. The deionized (DI) water through Millipore system (Milli-Q) with resistivity of ~18 MΩ cm^{-1} was used in the reactions.

2.2 Synthesis of the $CdCO_3/CdO/Co_3O_4$@NF electrode

The active composite material ($CdCO_3/CdO/Co_3O_4$) was synthesized directly on the nickel foam substrate through a hydrothermal-annealing process. First, the nickel foam was first cut into disk shaped pieces with 1.31 cm in diameter (1.35 cm^2 of geometrical area). The foam nickel samples have been washed in acetone for 10 min, and then etched in 1 M HCl for 10 min to remove the surface oxide layer, and finally rinsed several times with DI water. Further, in detail, 2 mmol of $Co(NO_3)_2 \cdot 6H_2O$, 2 mmol of $Cd(NO_3)_2 \cdot 6H_2O$ and 15 mmol of urea were mixed in 50 ml of deionized water, after 10 minutes of stirring, the obtained homogeneous reaction solution was transferred along with a piece of clean nickel foam into a Teflon-lined stainless steel reactor. It was sealed and maintained at 95 °C for 8 h, and then allowed to cool down to room temperature. The prepared sample was collected and rinsed with DI water several times. Then, the active material supported on the nickel foam was subjected to a heat treatment at 450 °C under an argon flow of 105 sccm for 3 h, to obtain the composite electrode. The resulting active material mass loaded onto the NF was about 0.008000 g. A microbalance MYA 2/3Y has been used. In the preparation of the other active compounds (*i.e.*: $CdCO_3$@NF, CdO@NF, $CdCO_3$/CdO@NF and $CdCO_3/CoCO_3$@NF), the synthetic route is similar, and experimental details are given in Table 1.

Table 1 Experimental synthesis conditions of the different chemical compounds to be electrochemical assayed as supercapacitor electrode materials. The employed nomenclature to individualize the different samples and to be used in the whole manuscript is also indicated

Hydrothermal bath composition	Hydrothermal temperature (°C)	Hydrothermal processing time (hours)	Annealing temperature (°C)	Annealing time (hours)	Annealing atmosphere	Structural phases present in the synthesized compound	Supercapacitor electrode material nomenclature
0.04 M $Cd(NO_3)_2$ + 0.3 M $CO(NH)_2$ [a]	95	8	w/o	w/o	w/o	$CdCO_3$	$CdCO_3$@NF
0.04 M $Cd(NO_3)_2$ + 0.3 M $CO(NH)_2$	95	8	450	3	O_2	CdO	CdO@NF
0.04 M $Cd(NO_3)_2$ + 0.3 M $CO(NH)_2$	95	8	450	3	Ar	$CdCO_3$ + CdO	$CdCO_3$/CdO@NF
0.04 M $Cd(NO_3)_2$ + 0.04 M $Co(NO_3)_2$ + 0.3 M $CO(NH)_2$ [b]	95	8	w/o	w/o	w/o	$CdCO_3$ + $CoCO_3$	$CdCO_3/CoCO_3$@NF
0.04 M $Cd(NO_3)_2$ + 0.04 M $Co(NO_3)_2$ + 0.3 M $CO(NH)_2$	95	8	450	3	Ar	$CdCO_3$ + CdO + Co_3O_4	$CdCO_3/CdO/Co_3O_4$@NF

[a] In brief: cadmium based bath. [b] In brief: cadmium + cobalt based bath.

2.3 Morphological, structural and surface chemistry characterization

The structural characterization of the composite material was carried out by X-ray diffraction (XRD) on a PAN analyticalX'Pert Pro automated diffractometer. Patterns were recorded in the Bragg–Brentano configuration using a monochromatic high intensity (Cu Kα1) radiation. An X'Celerator detector with a step size of 0.017° (2θ) was used, and the working power was 45 kV × 40 mA. Field emission scanning electron microscopy (FE-SEM) images of the electrodes were obtained on a Helios Nanolab 650 Dual Beam equipment from FEI Company. The analysis of the chemical composition of the formed structures was carried out using X-ray energy dispersion spectrometry (EDS). The equipment used was a QUANTAX 200 model from Bruker with XFLASH (EDX coupled to a SEM equipment: Hitachi SEM SU-3500 of variable pressure with a detector 410-M). Samples for TEM were prepared by removing the gridded nanostructured grown material with a scalpel, collected, and ultrasonically dispersed in 1 ml of ethanol. A small drop of the suspended solution was placed on a porous carbon film on a nickel screen and allowed to air dry. Transmission electron microscopy (TEM) and high-resolution transmission electron microscopy (HRTEM) images were obtained on a Talos F200X instrument.

The oxidation state of the chemical elements was studied *via* X-ray photoelectron spectroscopy (XPS) using an ESCA 5701 from Physical Electronics (PHI). An Al Kα radiation source (1486.6 eV) with an operating power of 400 W in an ultra-high vacuum system at a base pressure of $\sim 1.3 \times 10^{-8}$ Pa was employed. The XPS spectra have been corrected to C 1s at 284.8 eV.

2.4 Electrochemical characterization

The electrochemical behavior of the different synthesized electrode materials has been evaluated by cyclic voltammetry (CV), galvanostatic charge–discharge (GCD) measurements and electrochemical impedance spectroscopy (EIS) carried out at room temperature with an electrochemical workstation (PGSTAT 302A AUTOLAB). A three-electrode electrochemical cell set-up has been employed, where the electrode material under study acted as the working one and a 3 M Ag/AgCl and a platinum mesh as the reference and counter electrodes, respectively, in a 3 M KOH electrolytic solution. In order to avoid the presence of molecular oxygen in the electrolytic solutions, they were deaerated with Argon (Ar) for 20 minutes. During the measurements, an Ar stream was maintained over the solutions to ensure the absence of molecular oxygen in the solutions. EIS measurements were performed by applying an AC voltage with 10 mV amplitude in a frequency range from 0.1 Hz to 100 kHz at open circuit potential. Equivalent circuit modeling of the EIS spectrum has been analyzed by the Z-View Software.

The specific capacitance (capacitance per unit mass C_S (F g^{-1})) of the active material for the three-electrode configuration has been estimated from the CV experiments by using the following equation:[1,57,58]

$$C_S = \frac{\int I \mathrm{d}E}{2mv\Delta E} \quad (1)$$

where the integral represents the area enclosed by the CV curve, m is the mass of the electroactive material, v is the potential scan rate and ΔE denotes the potential window. The specific capacitance of the electrode has also been estimated by the charge–discharge analysis by using the following relation:[3,57,59]

$$C_S = \frac{2I\int E \mathrm{d}t}{m\Delta E^2} \quad (2)$$

where I is the constant discharge current, t is the discharge time, ΔE is the voltage window (excluding IR drop) and m is the mass of the active material.

A significant parameter for the investigation of the electrode material performance is the coulombic efficiency (η), which is the ratio of the discharge capacitance to the charge capacitance, and can be calculated *via* the following equation:[1,6]

$$\eta\ (\%) = \frac{C_{\text{discharge}}}{C_{\text{charge}}} \times 100 = \frac{t_{\text{discharge}}}{t_{\text{charge}}} \times 100 \quad (3)$$

where $C_{\text{discharge}}$ and C_{charge} are the discharge and charge capacitance, respectively and $t_{\text{discharge}}$ and t_{charge} are the discharge and charge time, respectively.

3 Results and discussion

3.1 Structural, morphological and surface chemical study

The preparation process of the different microstructured chemical compounds to be assayed as positive electrode materials for supercapacitors devices is illustrated in Scheme 1. First, commercial nickel foam was employed as the current collector to grow the chemical compound of interest *via* a hydrothermal step by using two different bath solutions (*i.e.*: a cadmium or a cadmium + cobalt-based solutions, see Experimental section for details); followed then by a high temperature post-annealing second step process in an oxygen or argon atmosphere. As it will be discussed further, according to the chosen route the final chemical compound or composite that is formed.

A review of the different obtained chemical compounds with a brief description of the followed synthesis procedure and with the nomenclature that will further used in this work, in order to identify the different studied samples, are depicted in Table 1.

In order to determine structural and morphological properties, the prepared compound samples have been characterized by X-ray diffraction (XRD), X-ray photoelectron spectroscopy (XPS), field emission-scanning electron microscopy (FE-SEM) and high-resolution transmission electron microscopy (HR-TEM). As revealed by XRD study (see Fig. 1a), the obtained compound after the hydrothermal process from a cadmium-based bath, is constituted exclusively by a cadmium carbonate ($CdCO_3$) single phase. In fact, the eight diffraction peaks at $2\theta = 23.5°$, 30.3°, 36.5°, 43.8°, 48.2°, 49.7°, 50.1° and 58.3° are corresponding to (012), (104), (110), (202), (024), (018), (116) and (122) crystallographic planes of rhombohedral cadmium carbonate,[60] respectively, have been well indexed. The two sharp diffraction peaks at $2\theta = 44.6°$ and 52.0° are characteristic peaks of nickel due to the presence of the Ni foam substrate.[61] The chemical reactions involved in the formation of this and the other hydrothermal compounds (*vide infra*) are given in the SI. The inset of Fig. 1a shows a FE-SEM high magnification micrograph of this sample, it can be seen that the chemical compound consisted in a randomly agglomeration of rhombohedral microcrystalline structures. As this rhombohedral phase of $CdCO_3$ has the same aspect of the rhombohedral phase of calcite ($CaCO_3$), both microcrystalline materials show similar structures (they look cubic at first glance);[20,62] then, indicating a morphology typically exhibited by the cadmium carbonate chemical compound, as has been reported in the literature.[20,62] Micro-particles exhibiting flat surfaces and sharp/round edges and corners with a mean size of about 5.8 μm can be observed. Those rhombohedral micro-particles are enclosed by {104} faces,[63–67] exhibiting roughened surfaces (a "sandblasted glass surface" aspect, *i.e.*: frosted glass aspect), due to the presence

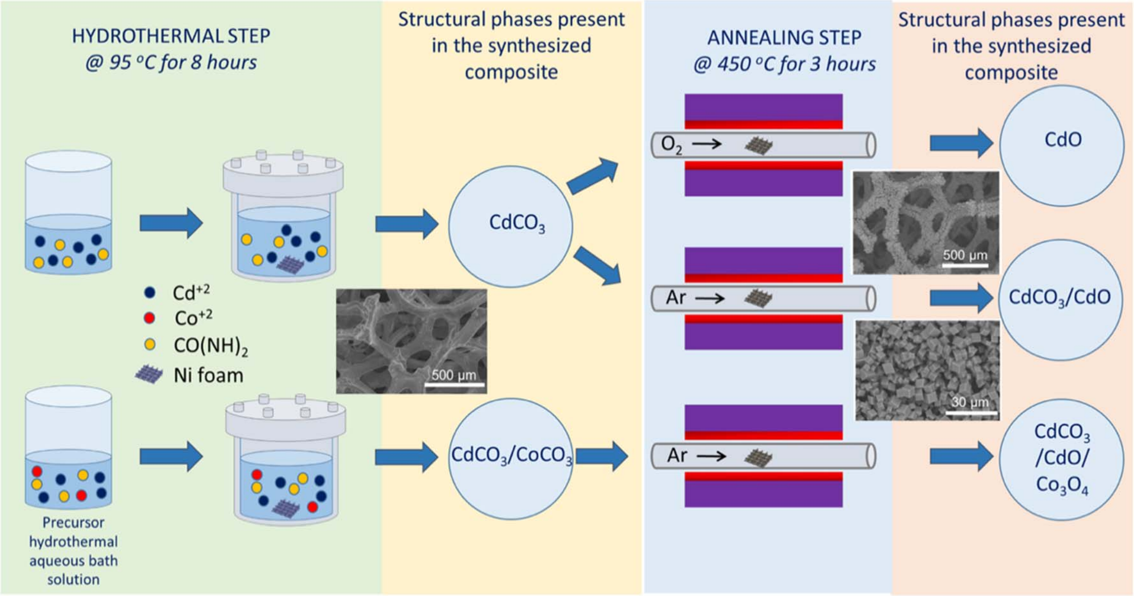

Scheme 1 Schematic illustration of the two-step process involved in the preparation of the different chemical compounds supported onto the nickel foam substrates. It is constituted by a first hydrothermal step followed by and annealing one. Two different hydrothermal baths (containing different precursors) and two different annealing atmospheres have been assayed. SEM micrograph on the left depicted a typical bare 3D nickel foam substrate, whereas those on the right illustrate (at two different magnifications), the typical cubic nanostructure exhibited by the synthesized composites grown onto this 3D nickel foam substrates.

very tiny nanoporous, fact that will be discussed later in this work (*vide infra*). Further, and as revealed by the XRD study, the obtained compound after the annealing process of this cadmium carbonate hydrothermal product sample (in an oxygen atmosphere), is constituted by a single cadmium oxide phase. The corresponding XRD pattern is depicted in Fig. 1b, where in addition to the diffraction peaks characteristics of the nickel foam, four diffraction peaks at the $2\theta = 33.0°$, 38.3°, 55.3° and 66.00° are ascribed to the (111), (200), (220) and (311) diffraction planes of cubic cadmium oxide,[68] respectively, can be observed. As can be seen in the inset of Fig. 1b, the agglomeration of micro-particles with 3D cubic shapes are formed, exhibiting flat smooth faces and well defined sharp edges and corners, with a mean size of about 3.0 µm. Typical crystal habit exhibited by a cadmium oxide compound obtained through calcination of a cadmium carbonate precursor.[69] When the sample obtained from a cadmium-based bath has been submitted to a heat treatment in an argon atmosphere, the formed compound is constituted by a minor cadmium carbonate phase and a major cadmium oxide one. The corresponding XRD pattern is depicted in Fig. 1c, where in addition to the diffraction peaks characteristics of the nickel foam, one diffraction peak at $2\theta = 23.5°$ corresponding to the (012) crystallographic plane of rhombohedral cadmium carbonate,[60] and four diffraction peaks at $2\theta = 33.0°$, 38.2°, 55.2° and 65.8° which are ascribed to the (111), (200), (220) and (311) diffraction planes of cubic cadmium oxide,[68] respectively, can be seen. A cube like micro structure can be observed (see a FE-SEM high magnification micrograph in the inset of Fig. 1c), with a mean size of about 3.7 µm, very similar to that exhibited by the compound after the annealing under an oxygen atmosphere (see inset of Fig. 1b), mainly due to the presence of the majority cadmium oxide phase. The XRD analysis of the final hydrothermal product from a cadmium + cobalt based bath, reflects that the formed compound is constituted by a minor cobalt carbonate phase and a major cadmium carbonate one. Fig. 1d displays the XRD pattern of this sample, wherein addition to the diffraction peaks characteristics of the nickel foam, two diffraction peaks at $2\theta = 32.6°$ and $2\theta = 51.4°$ corresponding to the (104) and (024) crystallographic planes of rhombohedral cobalt carbonate,[70] respectively; and nine diffraction peaks at the $2\theta = 23.6°$, 30.4°, 36.5°,43.9°, 48.2°, 49.6°, 50.1°, 58.3° and 62.0° are ascribed to the (012), (104), (110), (202), (024), (018), (116), (122) and (214) diffraction planes of rhombohedral cadmium carbonate,[60] respectively, can be seen. In addition, three diffraction peaks at $2\theta = 29.1°$, 47.3° and 69.6° appeared which, due to their low intensity; their identification is not a straightforward procedure. However, these diffraction peaks can be assigned to the formation of a trace amount of cobalt hydroxide carbonate ($Co_2(OH)CO_3$) phase,[71] which, as reported in the literature, under such hydrothermal conditions, it is very likely that it is forming.[5,47] In this case, the FE-SEM high-magnification micrograph image (see inset of Fig. 1d), reveals randomly orientated inter-grown rhombohedral microcrystals with flat roughened surfaces and sharp edges, and in some cases the corners are slightly truncated and rounded. Microcrystals exhibited a mean size of about 5.3 µm. Further and in the basis of the previously studies presented above, and in order to modulate the CdO content and to avoid a complete conversion of the hydrothermal compound to exclusively a cadmium oxide phase, the hydrothermal product from a cadmium + cobalt based bath has been annealed exclusively in an argon

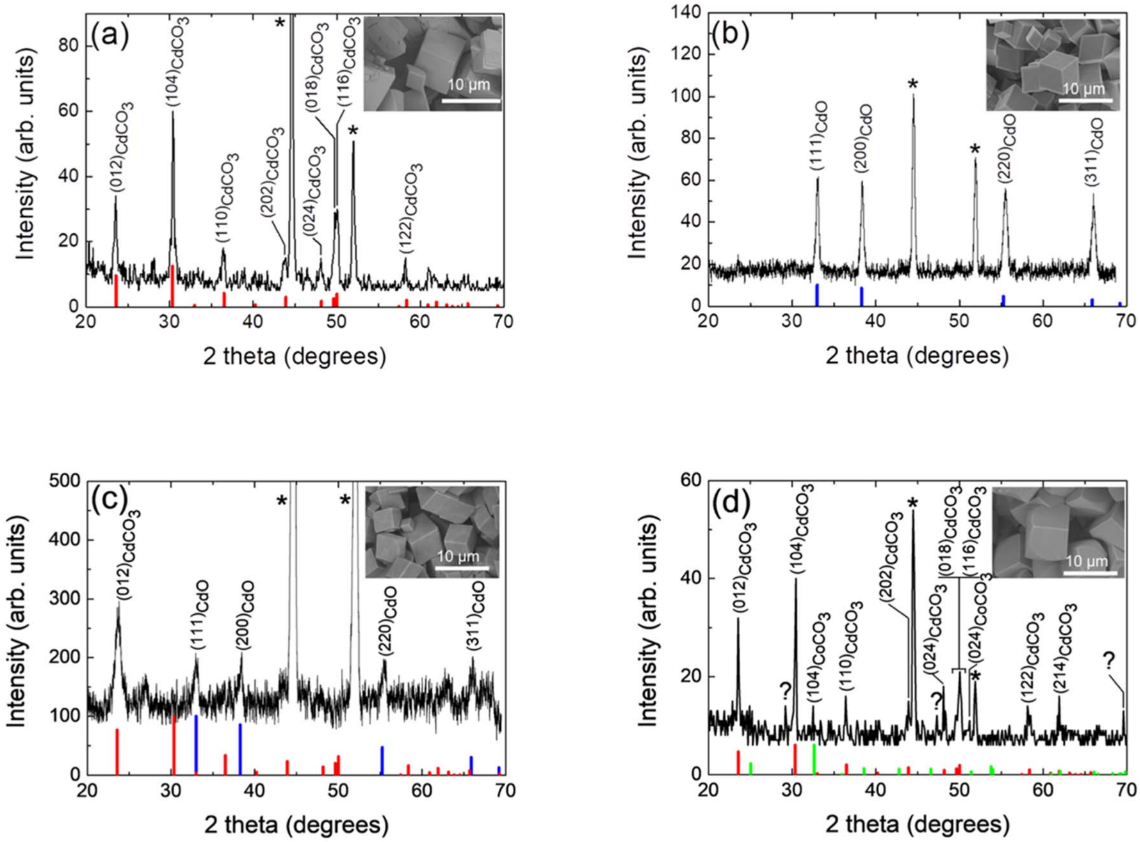

Fig. 1 X-ray diffraction pattern of the chemical compound hydrothermally grown onto a NF substrate from a solution containing cadmium and urea precursors: (a) as-grown ($CdCO_3$@NF); and after an additional annealing treatment in: (b) an oxygen atmosphere (CdO@NF) and (c) in an argon atmosphere ($CdCO_3$/CdO@NF). (d) X-ray diffraction pattern of the chemical compound hydrothermally grown onto a NF substrate from a solution containing cadmium, cobalt and urea precursors ($CdCO_3$/$CoCO_3$@NF). Rhombohedral cadmium carbonate (otavite), cubic cadmium oxide (monteponite) and rhombohedral cobalt carbonate (spherocobaltite) JCPDS patterns are also shown for comparison (thick red, blue and green bars, respectively). (*, indicates the peaks originated from the nickel foam substrate). Miller indices (*hkl*) for rhombohedral cadmium carbonate and cubic cadmium oxide diffraction planes are indicated. Insets: FE-SEM plan-view micrograph images, depicting the microcrystalline structure exhibited by these synthesized cadmium carbonate and cadmium oxide chemical compounds and two phase composite, according to the particulate case. The employed nomenclature to individualize each of the different samples is also indicated (see Table 1).

atmosphere. The corresponding XRD pattern is depicted in Fig. 2a, where in addition to the diffraction peaks characteristics of the presence of the nickel foam substrate, three diffraction peaks at $2\theta = 23.6°$, $2\theta = 30.3°$ and $2\theta = 43.9°$ corresponding to the (012), (104) and (202), diffraction planes, respectively, of rhombohedral cadmium carbonate,[60] and four diffraction peaks at $2\theta = 33.0°$, 38.2°, 55.2° and 65.8° which are ascribed to the (111), (200), (220) and (311) diffraction planes, respectively, of cubic cadmium oxide[68] can be observed. The last indicating that the compound is constituted at least by two main phases: cadmium carbonate and cadmium oxide ones. A TEM image of a nano-portion of the synthesized compound onto the nickel foam substrate and an EDS elemental mapping for the sample, which reveals the presence of Ni, Cd, and Co elements, are depicted in Fig. S1.† High resolution TEM image depicted in Fig. S1e† reveals three lattice fringes of 0.28, 0.24 and 0.46 nm, corresponding to (104), (200) and (111) lattice planes of rhombohedral phase of $CdCO_3$, cubic phase of CdO and cubic phase of Co_3O_4, respectively.[60,68,72] Fig. S1f† depicts the corresponding fast Fourier transform (FFT) pattern of this HRTEM result. The high-quality single-crystalline structure of the composite is demonstrated by the highly clear crystal lattice and the corresponding well-ordered dots pattern of the FFT image. Then, the presence of a Co_3O_4 phase has been proved. However, the lack of Co_3O_4 XRD peaks (as has been displayed above), can be due to the presence of a very small amount of this phase and/or that it is present with a low degree of crystallinity. It should be noted that X-ray diffraction statistically gives us a good idea of the average sample, whereas electron diffraction in TEM allows us to obtain local structure information. Fig. 2b depicts a low magnification FE-SEM micrograph image of this sample, showing that the compound densely and uniformly covers the skeleton surface of the nickel foam. It must be pointed out that this very good coverage is maintained even after the high temperature annealing step to which the samples have been subjected. Moreover, after being rinsed under centrifugation at 500 rpm for two minutes, the synthesized compound material remains well adhered to the nickel foam substrate, indicating that the binder-free integration is effective and robust. Although those encouraging properties are shown

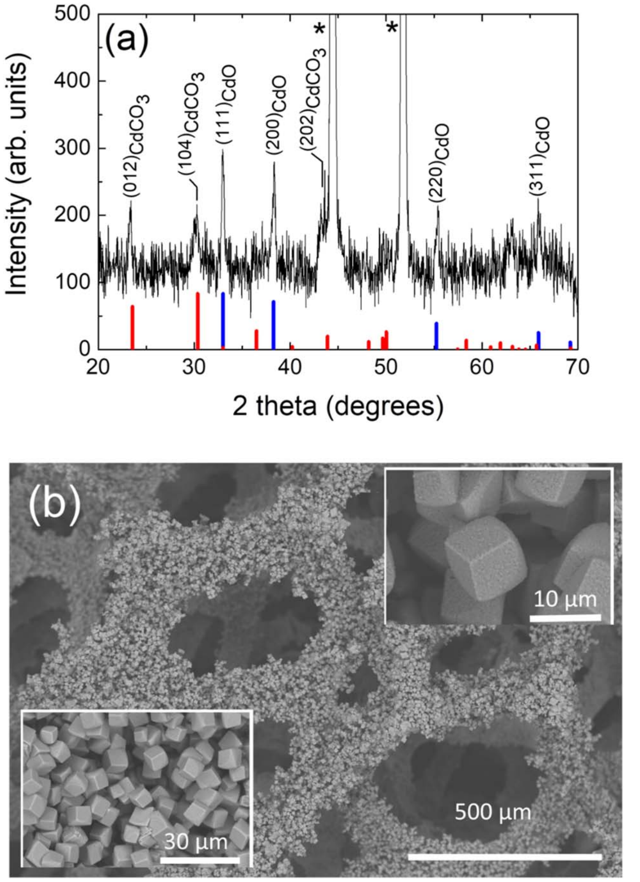

Fig. 2 (a) X-ray diffraction pattern of the chemical compound hydrothermally grown onto a NF substrate from a solution containing cadmium, cobalt and urea precursors after an additional annealing treatment in an argon atmosphere ($CdCO_3/CdO/Co_3O_4$@NF). Miller indices (*hkl*) for rhombohedral cadmium carbonate and cubic cadmium oxide diffraction planes are indicated. Rhombohedral cadmium carbonate (otavite) (thick red bars) and cubic cadmium oxide (monteponite) (thick blue bars) JCPDS patterns are also shown for comparison. (*, indicates the peaks originated from the nickel foam substrate). (b) FE-SEM plan-view micrograph image depicting the microcrystalline structure exhibited by this synthesized composite around the nickel foam substrate. The insets show high magnification FE-SEM plan-view micrograph images. The employed nomenclature to individualize this sample is also indicated (see Table 1).

for this particular case, it is observed for all the samples obtained under the different conditions studied in this work. The high-magnification FE-SEM micrograph images (see insets of Fig. 2b), reveal randomly orientated cubelike microcrystals with flat roughened surfaces and sharp edges with the corners slightly truncated and rounded. The presence of nanopores onto each of the faces can be observed. The generation and evolution of CO_2 as a result of the chemical decomposition of previously generated cadmium carbonate and the dehydration of cobalt hydroxide, both compounds formed during the hydrothermal phase process, could explain the occurrence of these nanopores.[47,51,69]

The surface chemical composition of the annealed hydrothermal product (from a cadmium + cobalt based bath), including the oxidation states and extent of surface impurities have been analyzed by X-ray photoelectron spectroscopy (XPS). XPS is a surface sensitive technique that can disclose elemental and chemical information about any solid material surface region.[73–76] The XPS survey spectrum of this compound is displayed in Fig. S2,† showing the presence of spectral peaks for C 1s, Cd $3d_{5/2}$, Cd $3d_{3/2}$, O 1s, Co 2p and Ni 2p (Ni signal coming from the Ni foam substrate), which is consistent with the above EDS elemental mapping results. Fig. S2† also shows that there are no additional elemental peaks, which demonstrates the high purity of the synthesized compound material and then correlating well with the XRD data. The core-level photoelectron spectra of Co 2p and O 1s along with the Gaussian fitting profiles are shown in Fig. S3a and b,† respectively. The Co 2p high-resolution spectrum (see Fig. S3a†) of the synthesized compound presents two main peaks at binding energies of 779.96 eV and 796.96 eV with a spin-energy separation of 17 eV. These two peaks correspond to Co $2p_{3/2}$ and Co $2p_{1/2}$ respectively which is characteristic of a Co_3O_4 phase.[34,77] Moreover, this is in line with the non-stoichiometric nature of the synthesized compound, indicating that cobalt can be present in two different oxidation states: Co^{2+} and Co^{3+} in a tetrahedral and octahedral environment of oxygen atoms, respectively. In fact, this spectrum can be deconvoluted into main four components ascribed to Co^{3+} $2p_{3/2}$, Co^{3+} $2p_{1/2}$, Co^{+2} $2p_{3/2}$ and Co^{2+} $2p_{1/2}$ at binding energies of 779.82 eV, 796.28 eV, 783.09 eV and 802.08 eV, respectively, all consistent with reported values in bibliography.[78,79] The high resolution spectrum of the O 1s (see Fig. S3b†) can be deconvoluted into three peaks. A strong peak at a binding energy of 529.37 eV is found and can be related to both the Cd–O and Co–O bonds, an identification of this peak is not straightforward as the corresponding tabulated binding-energy values are close to each other and its resolution is not easy, but as the atomic percentage of Co in the sample is minimum as said before, that peak could be assigned mainly to Cd–O bonds. The peak at 531.1 eV can be ascribed to $Cd–CO_3$, and the peak at a binding energy of 532.5 eV can be attributed to C–O bonds.[80,81] According to the Cd 3d signal, the high resolution spectrum showed $3d_{3/2}$ and $3d_{5/2}$ peaks at 412.7 and 405.97 eV, respectively (see Fig. S3c†). The deconvolution of the $3d_{5/2}$ peak into two peaks demonstrated the major presence of CdO *versus* $CdCO_3$, at binding energies of 406.02 and 405.47 eV, respectively.[80] It is also corroborated by C 1s signal, where CO_3^{-2} contribution is minimum (see Fig. S3d†), being the CdO/$CdCO_3$ ratio 2.05 (*i.e.*: CdO 67.2%, $CdCO_3$ 32.8%).

So, in addition to the presence of cadmium carbonate and cadmium oxide phases in the synthesized compounds, previously demonstrated by XRD (see above), then through the XPS analysis, the presence of a minor cobalt oxide phase has also been confirmed.

Then, in this work, tailoring the annealing step of the synthetic procedure (hydrothermal + annealing) it is has been possible to modulate the presence and amount of the electronic conductive CdO phase (which is formed at the expense of the previously hydrothermally synthesized $CdCO_3$ compound), which will enhance the electronic conductivity of the resulting compound.

3.2 Electrochemical performance of the different synthesized compounds

A three-electrode set-up has been next applied to systematically assess the electrochemical properties of the different synthesized electrode materials displayed in Table 1. As has been said above, a three-electrode setup is able to describe the electrochemical behavior of a tested material more properly than a two-electrode cell can, as is useful for a careful examination of the electrochemical properties of the electrode material.[15,17,52–56]

The comparison of the cyclic voltammetric responses shown in Fig. 3a indicates that is no significant contribution of the NF substrate to the electrochemical response exhibited by the different studied electrode materials. Moreover, the $CdCO_3/CdO/Co_3O_4$@NF electrode presents the highest cathodic and anodic peak current values and the largest associated integral area. In fact, this confirms the synergistic effect obtained by mixing the different phases considered. The response obtained indicates that the $CdCO_3/CdO/Co_3O_4$@NF electrode exhibits the greatest surface charge accumulation during the potential scan. A complex anodic and cathodic electrochemical response can be obtained when the potential scan rate is increased (see Fig. 3b). This is characterized by a slight displacement of the voltammetric peaks indicating an increase in the electrochemical irreversibility of the system. This observed displacement can be associated with the diffusional control of the electrolyte ions onto the nano/microporous architecture of the cubes, as well as the insertion of K^+ ions in the crystalline structure of $CdCO_3$. A specific capacity (C_S) of 1.003×10^3 F g^{-1} at 1 mV s^{-1} for this electrode can be calculated employing the eqn (1) (see Table S1† for C_S values at other potential scan rate values). The deconvolution of the potentiodynamic response of the $CdCO_3/CdO/Co_3O_4$@NF electrode shows a set of redox processes (see Fig. S4†). These correspond to the electrochemical reversible reactions of cobalt and cadmium that differ completely from an electrical double layer capacitor (EDLC) behavior and are more associated to a pseudocapacitive one. The kinetically reversible faradaic reactions involved in the electrochemical response of the electrode can be associated with the following couples: P_1/P_8 at 0.220 V and 0.266 V for Co^{2+}/Co^{3+} (see eqn (4)), P_4/P_5 at 0.320 V and 0.166 V for Co^{3+}/Co^{4+} (see eqn (5)),[82] P_2/P_6 at 0.244 V and 0.227 V for Cd^{2+}/Cd^{3+} in the CdO during reaction with hydroxyl ions (see eqn (6)).[83]

$$Co_3O_4 + OH^- + H_2O \leftrightarrows 3CoOOH + e^- \tag{4}$$

$$CoOOH + OH^- \leftrightarrows CoO_2 + H_2O + e^- \tag{5}$$

$$CdO + OH^- \leftrightarrows CdO(OH) + e^- \tag{6}$$

The redox couple designated by P_3/P_7 at 0.260 V and 0.190 V can be explained through two possibilities: (i) the partial reduction of the carbon that leads to the formation of elemental carbon (C^0) or low valence carbon (C^{2+})[20,84,85] and (ii) the presence of a low quantity of NiO formed on the clean NF surface not covered by the active $CdCO_3/CdO/Co_3O_4$ material during the annealing step. In our case, the NiO can be verified through a cyclic voltammetry study carried out from a clean NF and another undergone the same annealing process that $CdCO_3/CdO/Co_3O_4$ electrode (see Fig. S5†). The anodic and cathodic peaks observed in the 3 M KOH solution demonstrate the formation of NiO according to the reaction: $NiO + OH^- \leftrightarrows NiOOH + H_2O + e^-$.[86] In any case, a negligible contribution of NiO to the capacitance of the electrode should be expected.

The $CdCO_3/CdO/Co_3O_4$@NF electrode has been further characterized through an electrochemical impedance spectroscopy (EIS) study (see Fig. 4).[87] The Nyquist diagram shows a first semicircle in the high-frequency region (see inset of Fig. 4a) and then a pseudocapacitive behavior in the low-frequency zone.[88] The obtained experimental response has been simulated through a Randles circuit depicted as inset in Fig. 4a. This circuit considers the resistance of the solution (R_s), two constant phase elements (CPE1 and CPE2) attributed to the surface irregularities and the nano/microporous nature of the electrode material, two charge transfer resistances (R_{ct} and R_{pt})

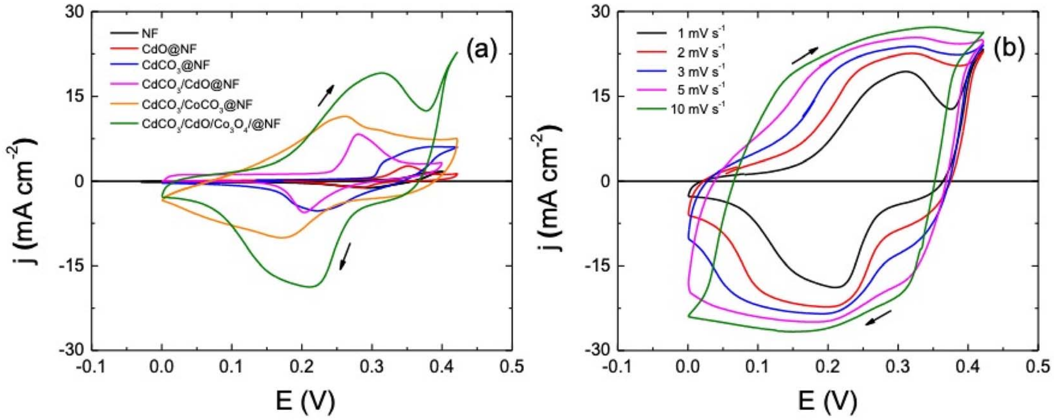

Fig. 3 (a) Cyclic voltammetric responses of the different studied electrodes: bare NF, CdO@NF, $CdCO_3$@NF, $CdCO_3/CdO$@NF, $CdCO_3/CoCO_3$@NF and $CdCO_3/CdO/Co_3O_4$@NF, as indicated, recorded at a potential scan rate of 1 mV s^{-1}. (b) Cyclic voltammetry of the $CdCO_3/CdO/Co_3O_4$@NF electrode at different potential scan rate values, as indicated. Electrochemical studies have been performed in a 3 M KOH electrolytic solution.

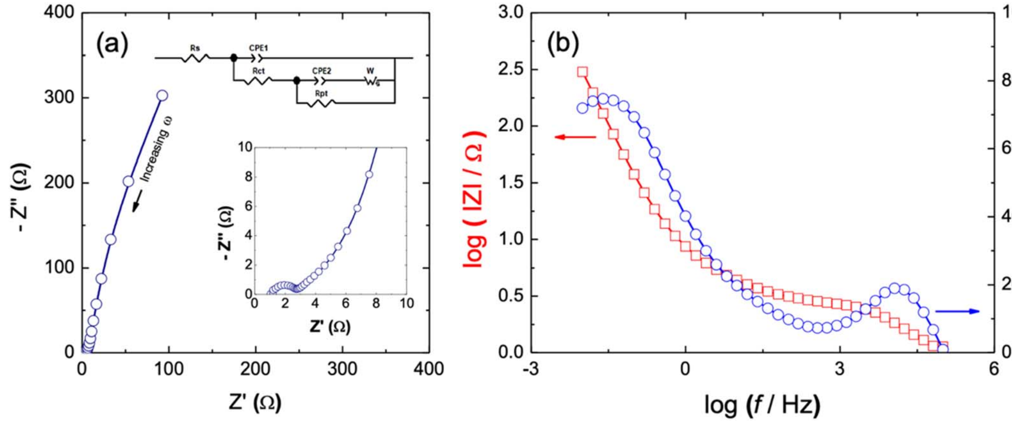

Fig. 4 (a) Nyquist and (b) Bode plots for the $CdCO_3/CdO/Co_3O_4$@NF electrode at an applied bias potential of −0.129 V. The symbols (open circle shapes) stand for experimental data and the solid lines are the curves fitted to the electrical circuit model depicted in the inset of panel (a). Electrochemical studies have been performed in a 3 M KOH electrolytic solution. The upper inset of panel (a) shows the equivalent electronic circuit model used to fit the experimental EIS data, whereas the lower one shows an enlargement of the Nyquist plot in the high-frequency range.

and a Warbug element (Wo).[87] The values obtained by simulation of Randles circuit are summarized in Table 2. The low R_s value indicates the good contact at the electrode/electrolyte interface.[87,88] The value obtained for CPE1 and R_{ct} indicates a predominant faradaic charge transfer process through the $CdCO_3/CdO/Co_3O_4$ compound in the double layer region. This contrasts with the higher values obtained for CPE2 and R_{pt} that can be associated to faradaic and non-faradic processes into the nano/microporous surface in the electrode structure.[87] The last indicates a good capacitive performance with short ion diffusion path in the supercapacitor device. This observation is supported from the fitting data of Warburg element that considers the Warburg resistance (WR), the time constant (WT) and the Warburg exponent (W-P). The obtained value of W-P = 0.50 confirms the mass control transport into the internal surface core of the $CdCO_3/CdO/Co_3O_4$ porous morphology that is consistent with what was previously observed through SEM images.[87] Fig. 4b shows the Bode plot to $CdCO_3/CdO/Co_3O_4$@NF electrode. The impedance exhibits a low value in the high frequency zone in contrast to those reported for other metallic carbonates.[89] This value can be associated to both a higher ionic and electronic conductivity related to the fast redox processes in the microcubes of the electrode material. In an ideal capacitive behavior and at low frequencies in the Bode plot, the phase angle should present values close to 90°.[87,88] A lower value than this would indicate the presence of a material with a charge accumulation mechanism due to both non-faradaic and faradaic contribution processes.[89] In the present case, the low frequency region of the Bode plot of the $CdCO_3/CdO/Co_3O_4$@NF electrode presents a phase angle value of 74.69°. This indicates that the charge storage mechanism can be due to both the accumulation of ions at the electrode/electrolyte interface and a small contribution from faradaic processes. This confirms the pseudocapacitive behavior of this active material.

The performance of the different electrode materials under study has been further evaluated by galvanostatic charge/discharge curves (GCD) at 1 mA cm^{-2} in this three-electrode set-up configuration (see Fig. 5a). In a first approach, the mass of active materials to the different electrode can be considered similar with respect to each other; in fact these values in mg are as follows: 7.260, 8.500, 7.400, 8.300 and 8.000 corresponding to CdO@NF, $CdCO_3$@NF, $CdCO_3/CdO$@NF, $CdCO_3/CoCO_3$@NF and $CdCO_3/CdO/Co_3O_4$@NF phases, respectively. As expected, the recorded GCD curves do not show the typical linear behavior associated with an EDLC. Considering this GCD response, the eqn (2) has been employed to determine its specific pseudo-capacitance[90–92] that are depicted in Table 3. The CdO@NF electrode exhibits a charge/discharge time lower than that showed for the $CdCO_3$@NF and $CdCO_3/CdO$@NF ones. The $CdCO_3$@NF electrode, does not present adequate symmetry in its GCD curves despite exhibiting long charge/discharge times. This behavior indicates that the $CdCO_3$@NF has a high resistance to charge transfer,[20] showing plateau-shaped curves that are characteristic of battery-type

Table 2 Equivalent circuit element values obtained through a complex non-linear least-squares fitting of the EIS spectra recorded for the $CdCO_3/CdO/Co_3O_4$@NF electrode at an applied bias potential of −0.129 V[a]

R_s (Ω)	CPE1(Ss^{α})	α_1[b]	R_{ct} (Ω)	CPE2(Ss^{α})	α_2[b]	R_{pt} (Ω)	WR	WT	W-P
1.137	2.08×10^{-5}	0.947	1.296	0.054	0.975	1654	16.130	3.085	0.50

[a] See inset of Fig. 4a for the involved electrical equivalent circuit. [b] The impedance of a CPE is defined as $Z_{CPE} = \frac{1}{Q(j\omega)^{\alpha}}$ where α $(0 < \alpha > 1)$ is an empirical constant with no real physical meaning.

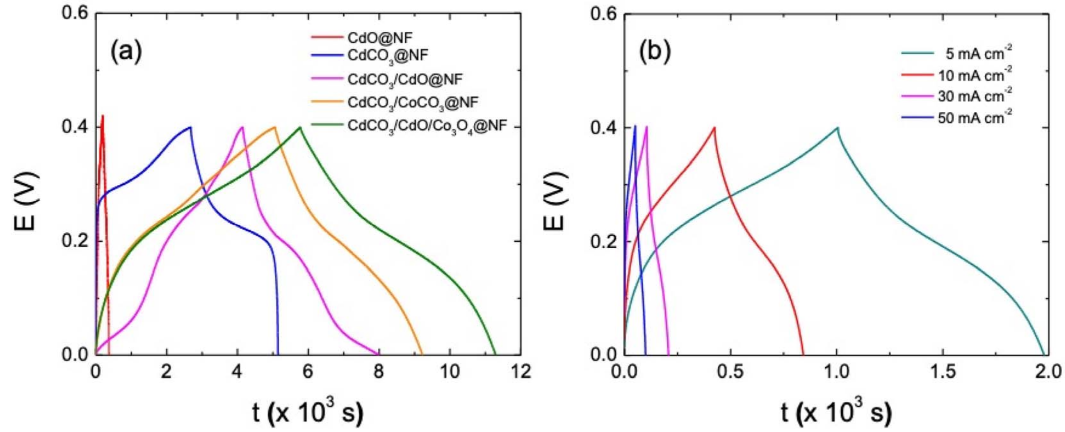

Fig. 5 (a) Galvanostatic charge and discharge curves of the: CdO@NF, CdCO$_3$@NF, CdCO$_3$/CdO@NF, CdCO$_3$/CoCO$_3$@NF and CdCO$_3$/CdO/Co$_3$O$_4$@NF studied electrodes, as indicated, recorded at 1 mA cm^{-2}. (b) GCD curves of the CdCO$_3$/CdO/Co$_3$O$_4$@NF electrode recorded at different current densities, as indicated. Electrochemical studies have been performed in a 3 M KOH electrolytic solution.

Table 3 Specific capacitance values obtained thorough GCD curves at a current density of 1 mA cm^{-2}. Electrode area 1 cm^2. Electrochemical studies have been performed in a 3 M KOH electrolytic solution

Electrode material	ΔV (V)	IR (mV)	C_S (F g^{-1})
CdO@NF	0.4	0.0	71.9
CdCO$_3$@NF	0.4	1.9	876.7
CdCO$_3$/CdO@NF	0.4	1.7	905.3
CdCO$_3$/CoCO$_3$@NF	0.4	1.3	1.175×10^3
CdCO$_3$/CdO/Co$_3$O$_4$@NF	0.4	1.4	1.759×10^3

electrodes.[90,91] However, when CoCO$_3$ and CdCO$_3$ are present forming the CdCO$_3$/CoCO$_3$@NF electrode, a better curve symmetry, an increase in the charge transfer of the system and an increasing in the charge/discharge times can be observed. The CdCO$_3$/CdO/Co$_3$O$_4$@NF electrode formed from the annealing of the CdCO$_3$/CoCO$_3$@NF presents a more significant improvement in: charge/discharge times (5479.5 s, excluding IR drop), capacitance value and GCD curve symmetry. The observed behavior shows the favorable charge transfer of this material compared to the CdCO$_3$/CoCO$_3$@NF one. This synergistic effect can be attributed to the presence of Co$_3$O$_4$, which increases the efficiency of the active sites of the base material.[93] As is depicted in Table 3, the specific capacitance values exhibited by those different compounds increases with the successively and sequentially addition of the others when passing from the single CdO compound to the final ternary CdCO$_3$/CdO/Co$_3$O$_4$ one. As it is expected, the CdO exhibits a very low specific capacitance value (71.9 F g^{-1}), as this material is not a typically capacitive material. On the other hand, the CdCO$_3$ exhibits a very good specific capacitance (876.7 F g^{-1}), due to its battery behavior. Further, a synergetic effect can be appreciated when the CdCO$_3$/CdO compound has been synthesized, exhibiting a specific capacitance of 905.3 F g^{-1}, which can be due an enhancement of to the electronic conductivity, given by the incorporation of the CdO phase. The CdCO$_3$/CoCO$_3$ binary compound exhibits a specific capacitance of 1.175×10^3 F g^{-1}, specific capacitance improvement due to the addition of the CoCO$_3$ battery type material. Finally, and due to the synergistic effect of the single compounds, *i.e.*: CdCO$_3$ (battery character), Co$_3$O$_4$ (pseudo-capacitance character) and CdO (electronic conductor material) an excellent specific capacitance of 1.759×10^3 F g^{-1} has been achieved with the ternary CdCO$_3$/CdO/Co$_3$O$_4$ compound. The GCD curves for the CdCO$_3$/CdO/Co$_3$O$_4$@NF electrode recorded between 5 mA cm^{-2} to 50 mA cm^{-2} are shown in Fig. 5b. The electrode shows stable behavior with a reversible redox capacitance and good pseudocapacitive performance. In fact, a 96% of coulombic efficiency can be calculated at highest current density (see Table S2†). The C_S values can be associated with different factors such as: morphology, porosity, surface area and the interconnectivity of the nano/microcubes. However, the decrease in C_S at high values of current density shows that the capacitance also depends on the ionic diffusion process through the mesopores compound morphology to access the internal surface of the material.

Fig. 6a shows the rate discharge capability and the coulombic efficiency of the CdCO$_3$/CdO/Co$_3$O$_4$@NF electrode at different current density values. The decrease in the specific capacitance with the increasing of the current density can be attributed to a poor internal diffusion process characterized by a short diffusion time of the ions through the pores to reach the inside of the material core. However, a C_S value of 792.3 F g^{-1} can be achieved at a current density of 50 mA cm^{-2}. On the other hand, the CdCO$_3$/CdO/Co$_3$O$_4$@NF electrode also demonstrates a high coulombic efficiency of 96% at a current density as high as 50 mA cm^{-2} (see Fig. 6a). The stability and life cycle performance of the electrode material has been tested by carrying out 1000 continuous GCD experiments at a current density of 10 mA cm^{-2}. Fig. 6b shows these GCD cycles indicating that the CdCO$_3$/CdO/Co$_3$O$_4$@NF electrode when a voltage window of 0.4 V was employed. The symmetry of the curves recorded throughout the 1000 cycles demonstrates the high stability and reversibility of the system. The incorporation of the

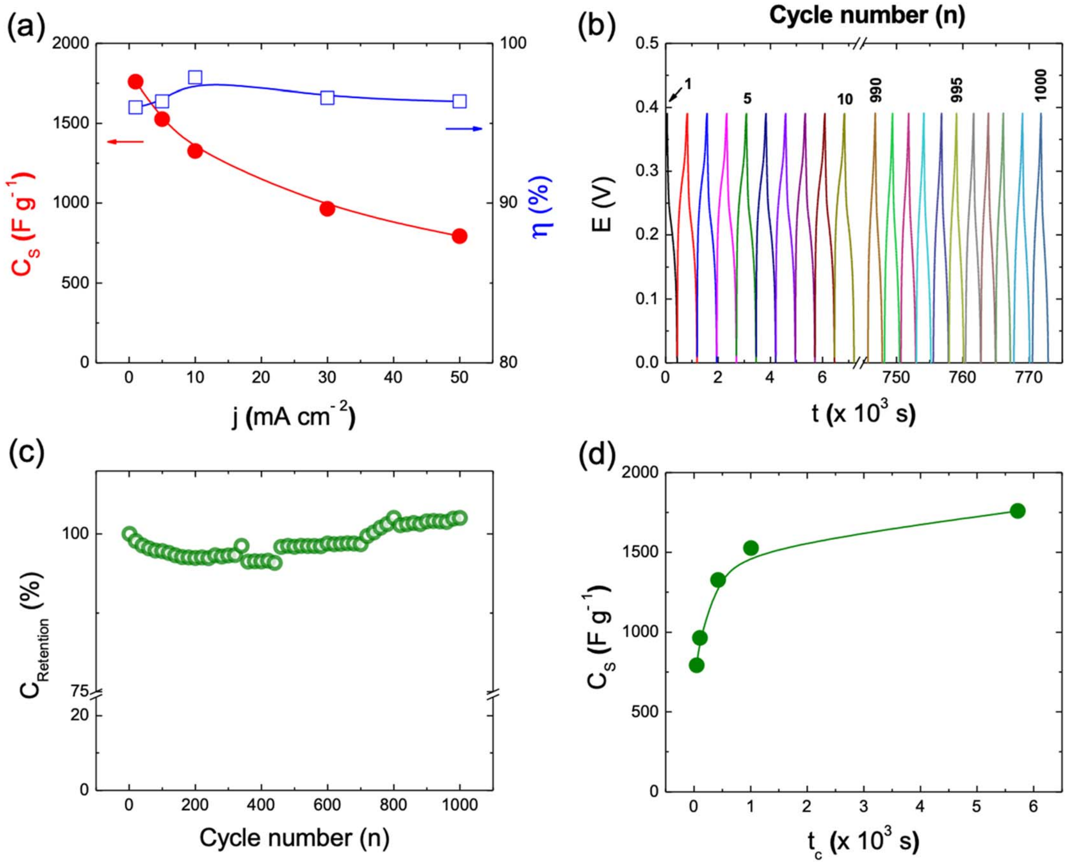

Fig. 6 Characterization of the $CdCO_3/CdO/Co_3O_4$@NF electrode as supercapacitor material. (a) The rate capability and the coulombic efficiency at different current densities. (b) Cycling performance through galvanostatic charge and discharge curves for a whole of 1000 cycles at the current density of 10 mA cm^{-2}. Cycle numbers are indicated. (c) Cycling stability of the electrode material after 1000 cycles from an initial 1326.2 F g^{-1} specific capacitance value. (d) Variation of the specific capacitance with the charging time of the material. These electrochemical studies have been performed in a 3 M KOH electrolytic solution.

CdO and Co_3O_4 phases to $CdCO_3$ efficiently improves the coulombic efficiency of the material. This contrasts with other materials employed in lithium-ion batteries that are based on $CdCO_3$ with carbon supports.[20] The retention capacitance with continuous GCD cycles is shown in Fig. 6c. This confirms the great stability of the electrode during the assayed 1000 cycles and without loss of active material. The retention capacitance remains around 100% until the 760 cycle and then increases to values greater than 100%. This phenomenon can be related to the activation processes of the material and has been previously reported in electrodes for supercapacitors based on CdS@NF.[51,57] To study the storage kinetics of the $CdCO_3/CdO/Co_3O_4$@NF electrode and its relationship with the nano/microporous morphology of the cubes of the electrode material, the dependence between C_S and charging time (t_c) for the different assayed current density values has been analyzed (see Fig. 6d).[57] Initially, the value of C_S increases with t_c whereas for longer charging times (lower density current values) a quasi-constant behavior can be appreciated. Moreover, it can be seen that the specific capacitance attains 45% of its maximum capacitance value in just 49.8 s. The last, indicating that in this first stage the faradaic mechanism contribution occurs on a short time scale (where ionic diffusion processes are not significant). Whereas, at longer times, a C_S maximum value of 87% has been achieved at 1000 s due to the role play by the interconnectivity of the microcubes as well as the poor ionic diffusion process (plateau of the C_S *vs.* t_c plot in Fig. 6d). This important total charge storage associated with the surface area has also been observed in other MnO_2-based electrodes where the 3D structure with interconnected channels favors an insertion/extraction process of the K^+ cations in the material.[94] In the $CdCO_3/CdO/Co_3O_4$@NF electrode this insertion/extraction process can be facilitated by the large size cavities that exist between the active material microcubes.[95]

4 Conclusions

In summary, a binder-free $CdCO_3/CdO/Co_3O_4$ compound with a cube-like morphology onto a nickel foam using a two-step hydrothermal + annealing procedure has been developed. Compound that exhibits superior performance with a high specific capacitance (C_S) of 1.759×10^3 F g^{-1} at a current density of 1 mA cm^{-2} and a C_S value of 792.3 F g^{-1} at a current density of 50 mA cm^{-2} with a rate capability of 43%. The $CdCO_3/CdO/Co_3O_4$@NF electrode also demonstrates a high coulombic efficiency of 96% at a current density as high as 50 mA cm^{-2} and also exhibits a good cycle stability with capacitance retention of *ca.* 100% after 1.000 cycles at a current density of 10 mA cm^{-2} along with a potential window of 0.4 V. The excellent electrochemical properties demonstrate the promising potential applications of the $CdCO_3/CdO/Co_3O_4$ compound material in supercapacitors devices.

Conflicts of interest

There are no conflicts to declare.

Acknowledgements

This work was partially supported by CSIC (Comisión Sectorial de Investigación Científica) of the Universidad de la República, in Montevideo, Uruguay, and PEDECIBA – Física, Uruguay. The Authors are grateful to Junta de Andalucia (Spain) through the research project UMA18-FEDERJA-039. The authors are also grateful for the support received from Consolidated DI project no 039.377/2021, PUCV, Chile.

References

1 R. Boddula, A. Khan, A. M. Asiri and A. E. Kolosov, *Handbook of Supercapacitor Materials*, Wiley-VCH, 2021.
2 K. K. Lee, W. S. Chin and C. H. Sow, *J. Mater. Chem. A*, 2014, **2**, 17212–17248.
3 A. Noori, M. F. El-Kady, M. S. Rahmanifar, R. B. Kaner and M. F. Mousavi, *Chem. Soc. Rev.*, 2019, **48**, 1272–1341.
4 P. Mone, S. Deore, S. Balgude and V. Pandit, *Mater. Today: Proc.*, 2022, **53**, 130–133.
5 X. Lin, H. Li, F. Musharavati, E. Zalnezhad, S. Bae, B.-Y. Cho and O. K. S. Hui, *RSC Adv.*, 2017, **7**, 46925–46931.
6 P. Xu, J. Liu, T. Liu, K. Ye, K. Cheng, J. Yin, D. Cao, G. Wang and Q. Li, *RSC Adv.*, 2016, **6**, 28270–28278.
7 K. K. Patel, T. Singhal, V. Pandey, T. P. Sumangala and M. S. Sreekanth, *J. Energy Storage*, 2021, **44**, 103366.
8 S. Vijayakumar, S. Nagamuthu and G. Muralidharan, *ACS Sustainable Chem. Eng.*, 2013, **1**, 1110–1118.
9 M. Zhang, Y. Wang, X. Guo, R. Li, Z. Peng, W. Zhang, Y. Zheng, H. Xie, Y. Zhang and Y. Zhao, *J. Electroanal. Chem.*, 2021, **897**, 115543.
10 Z. Yu, L. Tetard, L. Zhai and J. Thomas, *Energy Environ. Sci.*, 2015, **8**, 702–730.
11 Y. Wang, L. Hao, Y. Zeng, X. Cao, H. Huang, J. Liu, X. Chen, S. Wei, L. Gan, P. Yang, M. Liu and D. Zhu, *J. Alloys Compd.*, 2021, **886**, 161176.
12 Y. Yu, H. Wang, H. Zhang, Y. Tan, Y. Wang, K. Song, B. Yang, L. Yuan, X. Shen and X. Hu, *Electrochim. Acta*, 2020, **334**, 135559.
13 S. L. Kadam, S. M. Mane, P. M. Tirmali and S. B. Kulkarni, *Curr. Appl. Phys.*, 2018, **18**, 397–404.
14 Z. Liu, A. Qin, B. Yang, D. Wang and Z. Zhang, *Mater. Lett.*, 2019, **240**, 258–261.
15 S. M. Cha, S. Chandra Sekhar, R. Bhimanaboina and J. S. Yu, *Inorg. Chem.*, 2018, **57**, 8440–8450.
16 B. Pandit, L. K. Bommineedi and B. R. Sankapal, *J. Energy Chem.*, 2019, **31**, 79–88.
17 M. D. Stoller and R. S. Ruoff, *Energy Environ. Sci.*, 2010, **3**, 1294–1301.
18 C. Hao, X. Wang, X. Wu, Y. Guo, L. Zhu and X. Wang, *Appl. Surf. Sci.*, 2022, **572**, 151373.
19 P. J. Hall, M. Mirzaeian, S. I. Fletcher, F. B. Sillars, A. J. R. Rennie, G. O. Shitta-Bey, G. Wilson, A. Cruden and R. Carter, *Energy Environ. Sci.*, 2010, **3**, 1238–1251.
20 X. He, Z. Han, F. Kong, S. Tao, X. Jiang and B. Qian, *Mater. Lett.*, 2019, **236**, 672–675.
21 F. Zhang, R. Zhang, J. Feng and Y. Qian, *Mater. Lett.*, 2014, **114**, 115–118.
22 L. Shao, S. Wang, K. Wu, M. Shui, R. Ma, D. Wang, N. Long, Y. Ren and J. Shu, *Ceram. Int.*, 2014, **40**, 4623–4630.
23 Z. Ding, B. Yao, J. Feng and J. Zhang, *J. Mater. Chem. A*, 2013, **1**, 11200–11209.
24 L. Shao, R. Ma, K. Wu, M. Shui, M. Lao, D. Wang, N. Long, Y. Ren and J. Shu, *J. Alloys Compd.*, 2013, **581**, 602–609.
25 L. Su, Z. Zhou, X. Qin, Q. Tang, D. Wu and P. Shen, *Nano Energy*, 2013, **2**, 276–282.
26 H. Xuan, T. Liang, G. Zhang, Y. Guan, H. Li, R. Wang, P. Han and Y. Wu, *J. Alloys Compd.*, 2020, **818**, 153350.
27 P. Xu, K. Ye, D. Cao, J. Huang, T. Liu, K. Cheng, J. Yin and G. Wang, *J. Power Sources*, 2014, **268**, 204–211.
28 W. Guo, L. Hou, B. Hou and Y. Guo, *J. Alloys Compd.*, 2017, **708**, 524–530.
29 S. Ramesh, K. Karuppasamy, A. Sivasamy, H.-S. Kim, H. M. Yadav and H. S. Kim, *J. Alloys Compd.*, 2021, **877**, 160297.
30 R. Lakra, R. Kumar, P. K. Sahoo, D. Sharma, D. Thatoi and A. Soam, *Carbon Trends*, 2022, **7**, 100144.
31 M. Gaire, N. Khatoon and D. Chrisey, *Nanomater*, 2021, **11**, 717.
32 L. B. Kong, *Nanomaterials for Supercapacitors*, CRC Press, 2018.
33 Q. Yang, Z. Lu, X. Sun and J. Liu, *Sci. Rep.*, 2013, **3**, 3537.
34 C. Yuan, L. Yang, L. Hou, L. Shen, X. Zhang and X. W. (David) Lou, *Energy Environ. Sci.*, 2012, **5**, 7883–7887.
35 S. M. Abbas, S. T. Hussain, S. Ali, F. Abbas, N. Ahmad, N. Ali and Y. Khan, *J. Alloys Compd.*, 2013, **574**, 221–226.
36 A. Askarinejad and A. Morsali, *Chem. Eng. J.*, 2009, **150**, 569–571.
37 M. Ramazani and A. Morsali, *Ultrason. Sonochem.*, 2011, **18**, 1160–1164.
38 H. Liu, V. Avrutin, N. Izyumskaya, Ü. Özgür and H. Morkoç, *Superlattices Microstruct.*, 2010, **48**, 458–484.
39 A. Facchetti and T. J. Marks, *Transparent Electronics: From Synthesis to Applications*, John Wiley & Sons, Ltd, Chichester, UK, 2010.
40 P. A. Radi, A. G. Brito-Madurro, J. M. Madurro and N. O. Dantas, *Braz. J. Phys.*, 2006, **36**, 412–414.
41 B. Șahin, *Sci. World J.*, 2013, **2013**, 172052.
42 Y. Yang, S. Jin, J. E. Medvedeva, J. R. Ireland, A. W. Metz, J. Ni, M. C. Hersam, A. J. Freeman and T. J. Marks, *J. Am. Chem. Soc.*, 2005, **127**, 8796–8804.

43 J. S. Choi, Y. H. Kang and K. H. Kim, *J. Phys. Chem.*, 1977, **81**, 2208–2211.

44 J. Santos-Cruz, G. Torres-Delgado, R. Castanedo-Pérez, S. Jiménez-Sandoval, J. Márquez-Marín and O. Zelaya-Angel, *Sol. Energy*, 2006, **80**, 142–147.

45 T. D. Veal, P. D. C. King and C. F. McConville, in *Functional Metal Oxide Nanostructures*, ed. J. Wu, J. Cao, W. Han, A. Janotti and H. Kim, Springer, New York, NY, 2012, pp. 127–145.

46 U. Cvelbar, K. (Ken) Ostrikov and M. Mozetic, *Nanotechnology*, 2008, **19**, 405605.

47 H. Du, L. Jiao, Q. Wang, Q. Huan, L. Guo, Y. Si, Y. Wang and H. Yuan, *CrystEngComm*, 2013, **15**, 6101–6109.

48 B. Zhao, T. Wang, L. Jiang, K. Zhang, M. M. F. Yuen, J.-B. Xu, X.-Z. Fu, R. Sun and C.-P. Wong, *Electrochim. Acta*, 2016, **192**, 205–215.

49 L. Yu, G. Zhang, C. Yuan and X. W. (David) Lou, *Chem. Commun.*, 2013, **49**, 137–139.

50 B. Zhao, T. Wang, L. Jiang, K. Zhang, M. M. F. Yuen, J.-B. Xu, X.-Z. Fu, R. Sun and C.-P. Wong, *Electrochim. Acta*, 2016, **192**, 205–215.

51 R. Henríquez, A. S. Mestra-Acosta, E. Muñoz, P. Grez, E. Navarrete-Astorga and E. A. Dalchiele, *RSC Adv.*, 2021, **11**, 31557–31565.

52 V. Khomenko, E. Frackowiak and F. Béguin, *Electrochim. Acta*, 2005, **50**, 2499–2506.

53 H. Hua, S. Liu, Z. Chen, R. Bao, Y. Shi, L. Hou, G. Pang, K. N. Hui, X. Zhang and C. Yuan, *Sci. Rep.*, 2016, **6**, 20973.

54 Y. Zhou, P. Jin, Y. Zhou and Y. Zhu, *Sci. Rep.*, 2018, **8**, 9005.

55 V. Šedajová, P. Jakubec, A. Bakandritsos, V. Ranc and M. Otyepka, *Nanomaterials*, 2020, **10**, 1731.

56 C. Breitkopf and K. Swider-Lyons, *Handbook of Electrochemical Energy*, Springer, 2017.

57 I. Rathinamala, I. M. Babu, J. J. William, G. Muralidharan and N. Prithivikumaran, *Mater. Sci. Semicond. Process.*, 2020, **105**, 104677.

58 A. Yu, V. Chabot and J. Zhang, Electrochemical Supercapacitors for Energy Storage and Delivery. *Fundamentals and Applications*, CRC Press, Boca Raton, 2013.

59 J. Zhao and A. F. Burke, *Adv. Energy Mater.*, 2021, **11**, 2002192.

60 Powder diffraction file, Joint Committee for Powder Diffraction Studies (JCPDS) File No. 04-012-5237 (rhombohedral structure of $CdCO_3$).

61 Powder diffraction file, Joint Committee for Powder Diffraction Studies (JCPDS) File No. 04-0850 (cubic structure of Ni).

62 O. Portillo-Moreno, H. Lima-Lima, R. Lozada-Morales, R. Palomino-Merino and O. Zelaya-Angel, *J. Mater. Sci.*, 2005, **40**, 4489–4492.

63 H. Y. Kim, T. Yang, W. Huh, Y.-J. Kwark, Y. Lee and I. W. Kim, *Mater.*, 2019, **12**, 3339.

64 S. Kewalramani, G. Dommett, K. Kim, G. Evmenenko, H. Mo, B. Stripe and P. Dutta, *J. Chem. Phys.*, 2006, **125**, 224713.

65 A. Sengupta Ghatak, M. Koch, C. Guth and I. M. Weiss, *Int. J. Mol. Sci.*, 2013, **14**, 11842–11860.

66 G. Falini, S. Manara, S. Fermani, N. Roveri, M. Goisis, G. Manganelli and L. Cassar, *CrystEngComm*, 2007, **9**, 1162–1170.

67 R. R. Ruiz-Arellano and A. Moreno, *Cryst. Growth Des.*, 2014, **14**, 5137–5143.

68 Powder diffraction file, Joint Committee for Powder Diffraction Studies (JCPDS) File No. 01-073-2245 (cubic structure of CdO).

69 Y. Jia, X.-Y. Yu, T. Luo, J.-H. Liu and X.-J. Huang, *RSC Adv.*, 2012, **2**, 10251–10254.

70 Powder diffraction file, Joint Committee for Powder Diffraction Studies (JCPDS) File No. 04-008-8312 (rhombohedral structure of $CoCO_3$).

71 Powder diffraction file, Joint Committee for Powder Diffraction Studies (JCPDS) File No. 01-079-7085 (monoclinic structure of $Co_2(OH)_2(CO_3)$).

72 Powder diffraction file, Joint Committee for Powder Diffraction Studies (JCPDS) File No. 01-076-1802 (cubic structure of Co_3O_4).

73 C. K. Chua and M. Pumera, *Chem. – Eur. J.*, 2014, **20**, 1871–1877.

74 A. Foelske-Schmitz, in, *Encyclopedia of Interfacial Chemistry*, ed. K. B. T. Wandelt, Elsevier, Oxford, 2018, pp. 591–606, Hardcover ISBN: 9780128097397.

75 A. G. Marrani, A. Motta, F. Amato, R. Schrebler, R. Zanoni and E. A. Dalchiele, *Nanomaterials*, 2022, **12**, 43.

76 X. Chen, X. Wang and D. Fang, *Fullerenes, Nanotubes, Carbon Nanostruct.*, 2020, **28**, 1048–1058.

77 Z.-S. Wu, W. Ren, L. Wen, L. Gao, J. Zhao, Z. Chen, G. Zhou, F. Li and H.-M. Cheng, *ACS Nano*, 2010, **4**, 3187–3194.

78 S. Deng, X. Xiao, G. Chen, L. Wang and Y. Wang, *Electrochim. Acta*, 2016, **196**, 316–327.

79 Z. Zhu, W. Tian, X. Lv, F. Wang, Z. Hu, K. Ma, C. Wang, T. Yang and J. Ji, *J. Colloid Interface Sci.*, 2021, **587**, 855–863.

80 J. F. Moulder, W. F. Stickle, W. M. Sobol and K. D. Bomben, *Handbook of X-Ray Photoelectron Spectroscopy*, Perkin-Elmer Corporation, Physical Electronics Division, Eden Prairie, Minnesota (USA), 1992.

81 NIST XPS Database, **https://srdata.nist.gov/xps/main_search_menu.aspx**.

82 E. A. A. Aboelazm, G. A. M. Ali, H. Algarni, H. Yin, Y. L. Zhong and K. F. Chong, *J. Phys. Chem. C*, 2018, **122**, 12200–12206.

83 K. Dhamodharan, R. Yuvakkumar, V. Thirumal, G. Ravi, M. Isacfranklin, S. A. Alharbi, T. A. Alahmadi and D. Velauthapillai, *Ceram. Int.*, 2021, **47**, 30790–30796.

84 Y. Sharma, N. Sharma, G. V. S. Rao and B. V. R. Chowdari, *J. Mater. Chem.*, 2009, **19**, 5047–5054.

85 M. A. Garakani, S. Abouali, B. Zhang, C. A. Takagi, Z.-L. Xu, J. Huang, J. Huang and J.-K. Kim, *ACS Appl. Mater. Interfaces*, 2014, **6**, 18971–18980.

86 N. Duraisamy, A. Numan, S. O. Fatin, K. Ramesh and S. Ramesh, *J. Colloid Interface Sci.*, 2016, **471**, 136–144.

87 M. Jana, J. S. Kumar, P. Khanra, P. Samanta, H. Koo, N. C. Murmu and T. Kuila, *J. Power Sources*, 2016, **303**, 222–233.

88 A. Y. Chen, H. H. Liu, P. Qi, X. F. Xie, M. T. Wang and X. Y. Wang, *J. Alloys Compd.*, 2021, **864**, 158144.

89 M. Karuppaiah, R. Akilan, P. Sakthivel, S. Asaithambi, R. Shankar, R. Yuvakkumar, Y. Hayakawa and G. Ravi, *J. Energy Storage*, 2020, **27**, 101138.

90 S. Ashoka, P. Chithaiah and G. T. Chandrappa, *Mater. Lett.*, 2010, **64**, 173–176.

91 S. Zhang and N. Pan, *Adv. Energy Mater.*, 2015, **5**, 1401401.

92 B. Pandit, D. P. Dubal, P. Gómez-Romero, B. B. Kale and B. R. Sankapal, *Sci. Rep.*, 2017, **7**, 43430.

93 H. Gu, Q. Zhong, Y. Zeng, S. Zhang and Y. Bu, *J. Colloid Interface Sci.*, 2020, **573**, 299–306.

94 O. Ghodbane, J.-L. Pascal and F. Favier, *ACS Appl. Mater. Interfaces*, 2009, **1**, 1130–1139.

95 J. W. Kim, V. Augustyn and B. Dunn, *Adv. Energy Mater.*, 2012, **2**, 141–148.